Improved aeroelastic analysis framework to assess shear and cross-section deformability effects on static aeroelastic response

# Improved aeroelastic analysis framework to assess shear and cross-section deformability effects on static aeroelastic response

Rodolfo Azzara[1]*, Matteo Filippi[1]†, Marco Petrolo[1]‡, Riccardo Ricci[1]§, Giacomo Zecchin[1]¶

[1] MUL[2]*Lab*, Department of Mechanical and Aerospace Engineering, Politecnico di Torino, Corso Duca degli Abruzzi 24, 10129, Torino, Italy.

**Abstract:** *This research investigates the influence of shear and cross-section deformability on the static aeroelastic response of wings by applying a high-fidelity computational framework that couples Computational Fluid Dynamics (CFD) with refined one-dimensional (1D) and two-dimensional (2D) structural models based on the Carrera Unified Formulation (CUF). The framework incorporates low- and high-order beam and plate models to capture airfoil deformations, utilizing both Taylor and Lagrange expansion functions for the kinematics. Aerodynamic loads from the CFD model are transferred to the structural finite element model via the Infinite Plate Spline (IPS) method. The static aeroelastic response of various wing configurations, differing in aspect ratio, airfoil geometry, and sweep angle, is analyzed to assess aerodynamic loading calculation and the influence of elastic airfoil deformation. Comparisons with reference solutions and Vortex Lattice Method (VLM) results demonstrate the accuracy and reliability of the presented methodology, highlighting the importance of high-order models for accurate aeroelastic static response of aeronautical wings. The study further demonstrates the stabilizing effects of sweep angles in mitigating aeroelastic instabilities, providing valuable insights for aerospace design. The results establish the framework as a powerful tool for preliminary aircraft design, enabling efficient aeroelastic assessments using efficient 1D finite elements.*

**Keywords:** Finite Element Method; Carrera Unified Formulation; High-order models; Composites; CFD; Aeroelastic analysis.

## 1 Introduction

Aeroelasticity plays a crucial role in aeronautical engineering, as it governs the complex interaction between an elastic structure and the aerodynamic forces generated by airflow. Understanding and managing these interactions are essential for ensuring safety, optimizing performance, and enhancing the longevity of aerospace structures [1]. The need for accurate aeroelastic analyses has become increasingly important with the development of advanced aircraft featuring lightweight materials, high-aspect-ratio wings, and unconventional configurations. Given the weight constraints of modern aircraft, structures require greater flexibility, making aeroelasticity essential for studying phenomena like flutter, a dynamic instability where vibrations grow uncontrollably, and divergence, a static instability where structures deform increasingly under aerodynamic loads [2, 3]. The introduction of composite materials has added complexity to aeroelastic evaluations, but their high stiffness-to-weight ratio, fatigue resistance, and environmental stability make them very attractive for aerospace

*Assistant Professor. E-mail: rodolfo.azzara@polito.it

†Associate Professor. E-mail: matteo.filippi@polito.it

‡Associate Professor. E-mail: marco.petrolo@polito.it

§Graduate Student. E-mail: riccardo.ricci@studenti.polito.it

¶Graduate Student. E-mail: giacomo.zecchin@studenti.polito.it

applications. For a comprehensive overview of aeroelastic tailoring, readers are referred to Refs. [4, 5, 6].

In aircraft design, it is crucial to accurately assess the aeroelastic behavior of structural configurations, even in the preliminary stages. The availability of fast, robust, accurate, and reliable computational tools with predictive capabilities is desirable. This is especially true when a vast design space is available [7]. For instance, in modern aerospace structural design, the availability of composite materials offers designers a broad spectrum of combinations that would be prohibitively expensive to evaluate only through experimental testing [8]. These considerations drive the ongoing research into developing new computational tools for effective and accurate aeroelastic analyses. Consequently, various approaches for analyzing structures under aerodynamic loads, often categorized by the models used to describe both the structure and the aerodynamic field, are proposed in the literature. Generally, aeroelastic analyses fall under fluid-structure interaction (FSI) problems, necessitating the three-dimensional (3D) solution of fully coupled structural and fluid dynamics problems [9].

Although experimental testing remains essential, albeit costly, in certification procedures, the selection between alternative configurations in the conceptual and preliminary design phases is largely based on numerical modeling. This complements the experimental campaign and allows the exploration of the design space at reduced costs. To perform the aeroelastic analysis of a structural component, adequate aerodynamic and structural models and an algorithm to couple the two fields are needed [10]. Methods that couple fluids and structures using low-fidelity classical approaches, such as linear potential flow models and structural representations based on classical beam theories, are well-advanced. While these low-fidelity approaches are suitable for preliminary design, they are often not adequate for analyzing aircraft that experience complex flow/structure interactions. These scenarios require high-fidelity approaches, such as the computational fluid dynamics (CFD) for fluids directly coupled with high-fidelity finite element (FE) models for structures [11].

With the increasing interaction between aerodynamic, structural, and control disciplines in advanced aircraft, it is increasingly important to accurately predict the aerodynamic forces due to the wing and control surface deflection. The aerodynamic behavior has historically been challenging to predict analytically. Since the early works of Cicala [12], Ellenberger [13], Küssner [14], von Kármán [15], and Theodorsen [16], numerous models have been developed, ranging from strip theories to RANS equations [17, 18]. Strip theories, though efficient for preliminary design, neglect 3D effects and are limited to incompressible, inviscid flows at small angles of attack. The Vortex Lattice Method (VLM) improved predictions by capturing lift distribution, induced drag, and geometric effects [19], while the Doublet Lattice Method (DLM) extended these principles to unsteady compressible flow, proving essential for flutter analysis [20]. Despite the advancements of VLM and DLM, their reliance on linear potential flow theory means they cannot account for viscous effects, boundary layer separation, or transonic/supersonic shock waves, phenomena critical to real-world aircraft performance [21]. Advances in computing power have therefore enabled CFD [22], which provides high-fidelity aerodynamic loads and nonlinear flow behavior, coupled to structural models via interpolation methods, such as the Infinite Plate Spline (IPS) method [23], or other fluid-structure interaction strategies [24].

A considerable amount of research has been devoted to aeroelasticity since aeroelastic tailoring was developed to avoid divergence instability of wing structures [25]. In aeroelastic analysis, various structural modeling approaches have been adopted, including one-dimensional (1D) and two-dimensional (2D) models, which contribute to accurate aeroelastic evaluations but with a lower computational cost than solid models. The finite element method (FEM) is typically used to discretize the structure [26], allowing the derivation of governing equations in weak form and the solution of problems in algebraic form. In the literature, several aeroelastic studies have successfully employed beam and plate models coupled with low-fidelity aerodynamic methods such as the VLM or DLM. For instance, Weisshaar [27] discussed the static aeroelastic divergence characteristics of composite wings by using aerodynamic strip and laminated box beam models. Librescu and Song

[28] studied thin-walled anisotropic beams, including non-classical effects, to predict the static aeroelastic response and the divergence instability of swept-forward wings. Aeroelastic models to study the influence of directional properties of composite materials and non-classical effects on aeroelastic instabilities of thin-walled structures were developed by Qin and Librescu [29]. Murua *et al.* [30] presented the application of unsteady VLM in aircraft aeroelasticity. Dagilis and Kilikevicius [31] proposed an aeroelastic model for highly flexible aircraft based on rigid-body dynamics and VLM. Tamer and Maserati [32] performed estimates of the aeroelastic stability of control surfaces with nonlinearities. Gulizzi and Benendetti [33] carried out aeroelastic analyses of wings using a novel discontinuous Galerkin structural model coupled with the VLM. Benchmark models per practical aeroelastic optimization of aircraft wings were proposed by Gray and Martins [34]. These approaches are computationally efficient and widely used for preliminary design, but inherently neglect viscous effects and complex flow phenomena. In contrast, few works have explored the coupling of refined 1D structural models with high-fidelity CFD, despite the potential of such models to capture non-classical effects, such as warping, out- and in-plane deformations, torsion-bending coupling, or localized boundary conditions [35, 36, 37, 38]. These effects are important for accurate aeroelastic analyses. For instance, Gupta [39] performed aeroelastic analyses using finite element models coupled with CFD. A high-fidelity fluid-structure framework was proposed by Lyrio *et al.* [40] to study the static aeroelastic response in transonic flows. Aeroelastic tailoring of rotor blade structures using high-fidelity multidisciplinary design optimization was presented by Mangano *et al.* [41].

The aim of this work is to fill this gap by applying high-order 1D and 2D models based on the Carrera Unified Formulation (CUF) [42] in combination with CFD to investigate the role of shear and cross-section deformability in the static aeroelastic response. CUF is a hierarchical formulation in which refined models are obtained without ad-hoc formulations. Using this approach, the governing equations and the corresponding FE arrays of 1D and 2D theories are expressed in terms of Fundamental Nuclei (FNs), which represent the main building blocks of the presented methodology. In this research, the formulation is specifically applied to address aeroelastic analyses. Several papers have been recently published to extend CUF to fluid-interaction analyses by using refined models coupled with VLM [43, 44, 45], DLM [46, 47, 48] or CFD [49, 50]. In contrast, the present study integrates CUF with a high-fidelity CFD framework, enabling the direct numerical solution of the Reynolds-averaged Navier-Stokes (RANS) equations through an IPS-based interface. This advancement improves the accuracy of aerodynamic force predictions, especially in complex flow regimes. The novelty of this work lies in extending the framework to high-order beam models. Refined beam elements offer both computational advantages and greater modeling flexibility. Specifically, high-order beam models allow for the efficient representation of geometries with complex cross-sections, such as realistic airfoils, while capturing 3D stress states that classical formulations cannot reproduce. Although CFD typically dominates the computational cost, the use of 1D models yields significant efficiency gains, particularly in nonlinear regimes.

This article is structured as follows: (i) Section 2 presents the aeroelastic formulation, detailing the adopted structural and aerodynamic models as well as the fluid-interaction algorithm employed; (ii) then, Section 3 shows the numerical results; (iii) finally, some conclusions are given in Section 4.

## 2 Aeroelastic formulation

### 2.1 Structural model

The structural model integrates the CUF and FEM methodologies. Within the CUF framework, the generic 3D displacement field for beam and plate theories is represented as an expansion of generalized displacements.

$$
\begin{aligned}
&Beam: \quad \boldsymbol{u}(x,y,z) = F_\tau(x,z)\boldsymbol{u}_\tau(y), \qquad \tau = 1,\dots,M \\
&Plate: \quad \boldsymbol{u}(x,y,z) = F_\tau(z)\boldsymbol{u}_\tau(x,y), \qquad \tau = 1,\dots,M
\end{aligned}
\tag{1}
$$

in which $F_\tau$ stands for a set of functions of the cross-section coordinates $x$ and $z$ for beams and thickness expansion functions for plate models, respectively, $\boldsymbol{u}_\tau$ represents the generalized displacement vector, $M$ denotes the order of the expansion, and the repeated index $\tau$ stands for summation. For a comprehensive mathematical derivation of the 1D and 2D FEs within the CUF framework, readers are referred to [42]. In this study, both Lagrange (LE) and Taylor (TE) polynomials are employed as expansion functions for $F_\tau$. The acronym LE9 refers to the nine-point Lagrange polynomials, while TEN to a Taylor polynomial of order $N$. For clarity, the third-order Taylor expansion (TE3) for 1D models is reported below:

$$\begin{aligned}
u_x &= u_{x_1} + xu_{x_2} + zu_{x_3} + x^2u_{x_4} + xzu_{x_5} + z^2u_{x_6} + x^3u_{x_7} + x^2zu_{x_8} + xz^2u_{x_9} + z^3u_{x_{10}} \\
u_y &= u_{y_1} + xu_{y_2} + zu_{y_3} + x^2u_{y_4} + xzu_{y_5} + z^2u_{y_6} + x^3u_{y_7} + x^2zu_{y_8} + xz^2u_{y_9} + z^3u_{y_{10}} \\
u_z &= u_{z_1} + xu_{z_2} + zu_{z_3} + x^2u_{z_4} + xzu_{z_5} + z^2u_{z_6} + x^3u_{z_7} + x^2zu_{z_8} + xz^2u_{z_9} + z^3u_{z_{10}}
\end{aligned} \tag{2}$$

While an illustrative example of the interpolation function is reported below for the case of an LE9 beam model:

$$\begin{aligned}
F_\tau &= \frac{1}{4}(r^2 + rr_\tau)(s^2 + ss_\tau) && \tau = 1,3,5,7 \\
F_\tau &= \frac{1}{2}s_\tau^2(s^2 - ss_\tau)(1 - r^2) + \frac{1}{2}r_\tau^2(r^2 - rr_\tau)(1 - s^2) && \tau = 2,4,6,8 \\
F_\tau &= (1 - r^2)(1 - s^2) && \tau = 9
\end{aligned} \tag{3}$$

in which $r$ and $s$ range from $-1$ to $+1$, whereas $r_\tau$ and $s_\tau$ indicate the coordinates of the Lagrange points. A transformation is required to convert these natural coordinates into real coordinates $x-z$. The displacement model based on the LE may now be derived. Specifically, quadratic interpolation functions can be used as follows:

$$\begin{aligned}
u_x &= F_{u_x1}u_{x_1} + F_{u_x2}u_{x_2} + F_{u_x3}u_{x_3} + F_{u_x4}u_{x_4} + F_{u_x5}u_{x_5} + F_{u_x6}u_{x_6} \\
&\quad + F_{u_x7}u_{x_7} + F_{u_x8}u_{x_8} + F_{u_x9}u_{x_9} \\
u_y &= F_{u_y1}u_{y_1} + F_{u_y2}u_{y_2} + F_{u_y3}u_{y_3} + F_{u_y4}u_{y_4} + F_{u_y5}u_{y_5} + F_{u_y6}u_{y_6} \\
&\quad + F_{u_y7}u_{y_7} + F_{u_y8}u_{y_8} + F_{u_y9}u_{y_9} \\
u_z &= F_{u_z1}u_{z_1} + F_{u_z2}u_{z_2} + F_{u_z3}u_{z_3} + F_{u_z4}u_{z_4} + F_{u_z5}u_{z_5} + F_{u_z6}u_{z_6} \\
&\quad + F_{u_z7}u_{z_7} + F_{u_z8}u_{z_8} + F_{u_z9}u_{z_9}
\end{aligned} \tag{4}$$

Compared with classical theories, these models incorporate additional displacement components, including terms that account for thickness deformation. Such components are particularly relevant in FSI, as they enable the structural model to capture shear effects and cross-sectional deformability with greater fidelity, thereby enhancing the accuracy of aeroelastic predictions when coupled with CFD.

The FEM is used to approximate the longitudinal displacement vector for beams and the in-plane displacement vector for plates employing the shape functions,

$$\begin{aligned}
&Beam: && \boldsymbol{u}_\tau(y) = N_i(y)\boldsymbol{q}_{\tau i}, && i = 1,\dots,N_n \\
&Plate: && \boldsymbol{u}_\tau(x,y) = N_i(x,y)\boldsymbol{q}_{\tau i}, && i = 1,\dots,N_n
\end{aligned} \tag{5}$$

where $N_i$ represents the shape functions, while $\boldsymbol{q}_{\tau i}$ denotes the unknown nodal variables. The term $N_n$ corresponds to the number of nodes per element, and the index $i$ indicates summation. In this paper, classical 1D FEs with four nodes (B4), which employ cubic approximation along the beam axis, are utilized. Meanwhile, classical 2D FEs with nine-node quadratic (Q9) interpolation are adopted for the shape functions in the $x$-$y$ plane.

By combining the FE approximation in Eq. 5 with the CUF formulation in Eq. 1, the 3D displacement field is expressed as:

$$
\begin{aligned}
&Beam: \quad \boldsymbol{u}(x,y,z) = F_\tau(x,z)N_i(y)\boldsymbol{q}_\tau, \qquad \tau = 1,\dots,M \qquad i = 1,\dots,N_n \\
&Plate: \quad \boldsymbol{u}(x,y,z) = F_\tau(z)N_i(x,y)\boldsymbol{q}_\tau, \qquad \tau = 1,\dots,M \qquad i = 1,\dots,N_n
\end{aligned} \tag{6}
$$

To derive the static governing equations, the principle of virtual displacements (PVD) is employed.

$$
\delta L_{int} = \delta L_{ext} \tag{7}
$$

where $\delta L_{int}$ represents the internal virtual work due to the elastic forces, $\delta L_{ext}$ denotes the work of the external forces, and $\delta$ denotes virtual variations. Specifically, the variations of the internal and external work can be written in terms of the FNs of the stiffness matrix and the external load, as follows:

$$
\begin{aligned}
&\delta L_{int} = \textstyle\int_V \delta\boldsymbol{\epsilon}^{\mathrm{T}}\boldsymbol{\sigma} dV = \delta\boldsymbol{q}_{sj}^{\mathrm{T}}\boldsymbol{K}^{ij\tau s}\boldsymbol{q}_{\tau i} \\
&\delta L_{ext} = \delta\boldsymbol{q}_{\tau i}^{\mathrm{T}}\boldsymbol{F}^{\tau i}
\end{aligned} \tag{8}
$$

in which $\boldsymbol{\epsilon}$ and $\boldsymbol{\sigma}$ stand for the strain and stress vectors, and $\boldsymbol{F}$ contains the aerodynamic forces. Linear strain-displacement relations are used, while the stresses are computed from the constitutive relations.

$$
\boldsymbol{\epsilon} = \boldsymbol{b}u \tag{9}
$$

$$
\boldsymbol{\sigma} = \boldsymbol{C}\epsilon \tag{10}
$$

where $\boldsymbol{b}$ represents a linear differential operator, and $\boldsymbol{C}$ indicates the material elastic matrix. For a detailed description of these matrices, readers are referred to Ref. [26].

### 2.2 Aerodynamic model

The aerodynamic model employed in this study is based on the direct numerical resolution of the RANS equations using CFD. Specifically, CFD is the source for the aerodynamic loads applied to the flexible structure. The flow is analyzed within a discretized 3D control volume, where the surface growth mesh depends on the $y^+$ value. This non-dimensional parameter characterizes the viscous sub-layer, being directly proportional to the friction velocity $u_\tau$ and the dimensional distance from the wall $y$, while inversely proportional to kinematic viscosity $\nu$. It is expressed as:

$$
y^+ = \frac{y u_\tau}{\nu} \tag{11}
$$

To ensure the independence of the results, convergence tests must be conducted with respect to the value of $y^+$, the extent of the far-field relative to the model geometry, and the growth rate of the volume mesh within the viscous sub-layer. Comprehensive guidelines can be found in Ref. [51].

This work employs the open-source SU2 solver [52], based on the Finite Volume Method (FVM), for aerodynamic predictions. Boundary conditions are defined on the surface to identify the impermeable wall, i.e., the wing surface, the far-field, where asymptotic flow conditions are imposed, and potentially symmetry conditions, which help reduce computational cost. The laminar model and the Spalart-Allmaras (SA) turbulence model [53] are adopted in this work. The SA model, in particular, introduces an additional transport equation for turbulent viscosity.

For RANS simulations, accurately resolving the viscous sub-layer requires appropriate grid refinement near the wall. Specifically, a sufficient number of cells must be included within the viscous sub-layer. The literature suggests selecting the height of the first cell $\Delta s$ such that $y^+$ remains below unity. However, since the exact value of $y^+$ is unknown a priori, the necessary $\Delta s$ can be estimated using the boundary layer theory for a flat plate. Through the following analytical formulas, it is possible to determine the Reynolds number (Re), the wall friction coefficient $c_f$, the wall shear stress $\tau_w$, and the size of the first cell:

$$Re = \frac{\rho V L}{\mu}, \quad c_f = 0.026 Re^{-\frac{1}{7}}, \quad \tau_w = \frac{c_f \rho V_\infty^2}{2}, \quad \Delta s = \frac{y^+ \mu}{\sqrt{\frac{\tau_w}{\rho}}\rho} \tag{12}$$

where $L$ represents a characteristic length in the $x$-direction. Once the simulation is completed, it is necessary to verify that the obtained flow field is plausible and that the calculated value of $y^+$ aligns with expectations. If these checks fail, further refinement of the computational grid near the wall is required.

Once the aerodynamic field is solved, the forces per unit area $\bar{\boldsymbol{t}}(\bar{\boldsymbol{x}})$ acting on the wing surface can be computed as follows:

$$\bar{\boldsymbol{t}}(\bar{\boldsymbol{x}}) = \frac{1}{2}\rho_\infty V_\infty \boldsymbol{c}(\bar{\boldsymbol{x}})\boldsymbol{n}(\bar{\boldsymbol{x}}) \tag{13}$$

in which $\boldsymbol{c}(\bar{\boldsymbol{x}})$ stands for the vector collecting the pressure coefficient $c_p$ and skin friction coefficient $c_{f_{x_i}}$, and $\boldsymbol{n}(\bar{\boldsymbol{x}})$ denotes the unit normal vector at a considered point $\bar{x}$ inside the surface.

### 2.3 Fluid-structure interaction

The FSI algorithm facilitates bidirectional transfer of aerodynamic forces from the aerodynamic to the structural mesh, and of structural displacements from the structural to the aerodynamic mesh, for an updated CFD analysis. To ensure accuracy, both transformations must be performed conservatively. In this study, the IPS technique was employed to interpolate quantities between the aerodynamic and structural grids. Fluid stresses could be applied directly as boundary conditions on the contour of the elastic domain. This would require extracting the pressure distributions from the aerodynamic mesh and then redistributing them into the structural mesh using shape and expansion functions. However, this procedure would be extremely time-consuming, as it must be performed individually for all structural nodes. In contrast, the IPS method provides an efficient interpolation strategy that automatically transfers loads between non-corresponding grids, ensuring accuracy and avoiding the computational overhead of node-by-node mapping.

This mathematical technique is used to fit a function $w$ over a surface defined by coordinates $(x,\, y)$ based on known function values at a discrete set of points. This theory considers an infinite plate of constant thickness and solves its equilibrium differential equations, obtaining a closed-form solution that satisfies deflections at the structural points. Once the system of linear equations is solved, the deflections at the aerodynamic points can be determined. A set of $N_{PS}$ pseudo-structural points is defined as the target locations for aerodynamic load transfer. The number of aerodynamic grid points on the body's surface, where the loads are applied, is denoted as $N_{AP}$. The equilibrium equation for a plate with flexural stiffness $D$, subjected to a distributed load $q$, is written as:

$$D\Delta^4 w = q \tag{14}$$

where $w$ represents the plate deflection. Eq. 14 can be rewritten in polar coordinates as follows:

$$D\frac{1}{r}\frac{d}{dr}\{r\frac{d}{dr}[\frac{1}{r}\frac{d}{dr}(r\frac{dw}{dr})]\} = q \tag{15}$$

The solution of the homogeneous differential equation has the following form:

$$w(r) = C_0 + C_1 r^2 + C_2 \ln r + C_3 r^2 \ln r \tag{16}$$

in which $C_0$, $C_1$, $C_2$, and $C_3$ denote the integration constants.

For a plate subjected to $N$ concentrated loads applied at points $(x_i,\, y_i)$, with $i = 1, \ldots, N$, the final expression that allows us to determine the deflection at a generic point can be written as:

$$w(x,y) = a_0 + a_1 x + a_2 y + \sum_{i=1}^{N} F_i K_i(x,y) \tag{17}$$

with

$$K_i(x, y) = r_i^2 \ln r_i^2 \tag{18}$$

In this equation there are $N + 3$ unknowns, namely the $N$ and $F_i$ values and the coefficients $a_0$, $a_1$ and $a_2$. To determine the deflection field, an equivalent number of equations must be formulated. The equilibrium boundary conditions provide three equations. By considering the loads applied at the pseudo-structural points $N = N_{PS}$, and assuming the transverse displacements at these points are known, it is possible to write $N_{PS}$ equations for the calculation of $w_j$, with $j = 1, \dots, N_{PS}$. In compact form:

$$\begin{bmatrix} \mathbf{0} \\ \boldsymbol{w} \end{bmatrix} = \begin{bmatrix} \mathbf{0} & \boldsymbol{R}^{\mathrm{T}} \\ \boldsymbol{R} & \boldsymbol{K} \end{bmatrix} \begin{bmatrix} \boldsymbol{a} \\ \boldsymbol{F} \end{bmatrix} = \boldsymbol{G} \begin{bmatrix} \boldsymbol{a} \\ \boldsymbol{F} \end{bmatrix} \tag{19}$$

where $\boldsymbol{G}$ is a square matrix of dimensions $(N_{PS} + 3) \times (N_{PS} + 3)$, which can be easily computed using the predefined coordinates of the pseudo-structural points. From Eq. 19 the values of the unknowns $\boldsymbol{a}$ and $\boldsymbol{F}$ can be determined. Once the spline coefficients are known, the deflection at each point on the plate can be evaluated. For the $N_{AP}$ points of the aerodynamic grid, a corresponding set of $N_{AP}$ equations can be formulated for the calculation of $w_k^*$, where $k = 1, \dots, N_{AP}$.

$$w_k^* = w(x_k, y_k) = a_0 + a_1 x_k + a_2 y_k + \sum_{i=1}^{N} F_i K_{ki} \tag{20}$$

Formulating the equation to compute the transverse displacement for all $N_{AP}$ aerodynamic points results in the following system:

$$\boldsymbol{w}^* = \boldsymbol{D}\boldsymbol{G}^{-1} \begin{Bmatrix} \mathbf{0} \\ \boldsymbol{w} \end{Bmatrix} \tag{21}$$

where $\boldsymbol{w^*}$ represents the vector of the deflection in the aerodynamic points. The matrix $\boldsymbol{D}$ of dimensions $N_{AP} \times (N_{PS} + 3)$ is:

$$\boldsymbol{D} = \begin{bmatrix} 1 & x_{1_{AP}} & y_{1_{AP}} & K_{1_{AP},1} & K_{1_{AP},2} & \cdots & K_{1_{AP},N_{PS}} \\ 1 & x_{2_{AP}} & y_{2_{AP}} & K_{2_{AP},1} & K_{2_{AP},2} & \cdots & K_{2_{AP},N_{PS}} \\ \vdots & \vdots & \vdots & \vdots & \vdots & \ddots & \vdots \\ 1 & x_{N_{AP}} & y_{N_{AP}} & K_{N_{AP},1} & K_{N_{AP},2} & \cdots & K_{N_{AP},N_{PS}} \end{bmatrix} \tag{22}$$

Therefore, it is possible to obtain a relation that links the displacements $w^*$ and $w$:

$$\boldsymbol{w^*} = \boldsymbol{D}\boldsymbol{G'}^{-1}\boldsymbol{w} = \boldsymbol{T}\boldsymbol{w} \tag{23}$$

in which $\boldsymbol{T}$ stands for the interpolation matrix, $\boldsymbol{G'}^{-1}$ represents the $\boldsymbol{G}^{-1}$ excluding its first three columns. Once the relationship between the deflections in the aerodynamic grid $\boldsymbol{w_k}$ and those in the structural mesh $\boldsymbol{w_s}$ is established, the corresponding connection between the loads applied in the two computational grids can be derived.

$$\boldsymbol{w_k} = \boldsymbol{T}\boldsymbol{w_s} \tag{24}$$

Similarly, the relationship between the aerodynamic force vector and the load vector at the pseudo-structural points is obtained. This formulation defines the relationship used to transfer the loads from the aerodynamic grid to the structural grid.

$$\boldsymbol{F_s} = \boldsymbol{T}^{\mathrm{T}}\boldsymbol{F_k} \tag{25}$$

The aeroelastic problem is solved through an iterative procedure. This iterative method consists of several phases:

1. **Aerodynamic solution (undeformed body)**: The aerodynamic software calculates the flow field around the body. The *SU2_CFD* tool requires a configuration file containing the aerodynamic mesh, upstream flow conditions, boundary conditions, and numerical methods. The iterations proceed until the specified convergence condition is reached;
2. **IPS Method**: The IPS algorithm transfers structural loads from the aerodynamic grid to the pseudo-structural points of the structural mesh;
3. **Structural solution**: The CUF+FEM approach allows to determine the structure's deformations under aerodynamic loading;
4. **Deformation of the aerodynamic mesh**: The outputs of the structural analysis (displacement field) update the input file of the *SU2_DEF* tool;
5. **Aerodynamic solution (deformed body)**: The aerodynamic software recalculates the flow field around the deformed body. The *SU2_CFD* tool takes the modified aerodynamic mesh as a new input and generates a new pressure distribution as an output. The iterative procedure then resumes from phase 2.

The procedure is repeated until convergence is achieved, specifically in terms of displacement at the leading edge of the wing tip section. For clarity, a schematic representation of the iterative method employed in solving the aeroelastic problem is shown in Fig. 1.

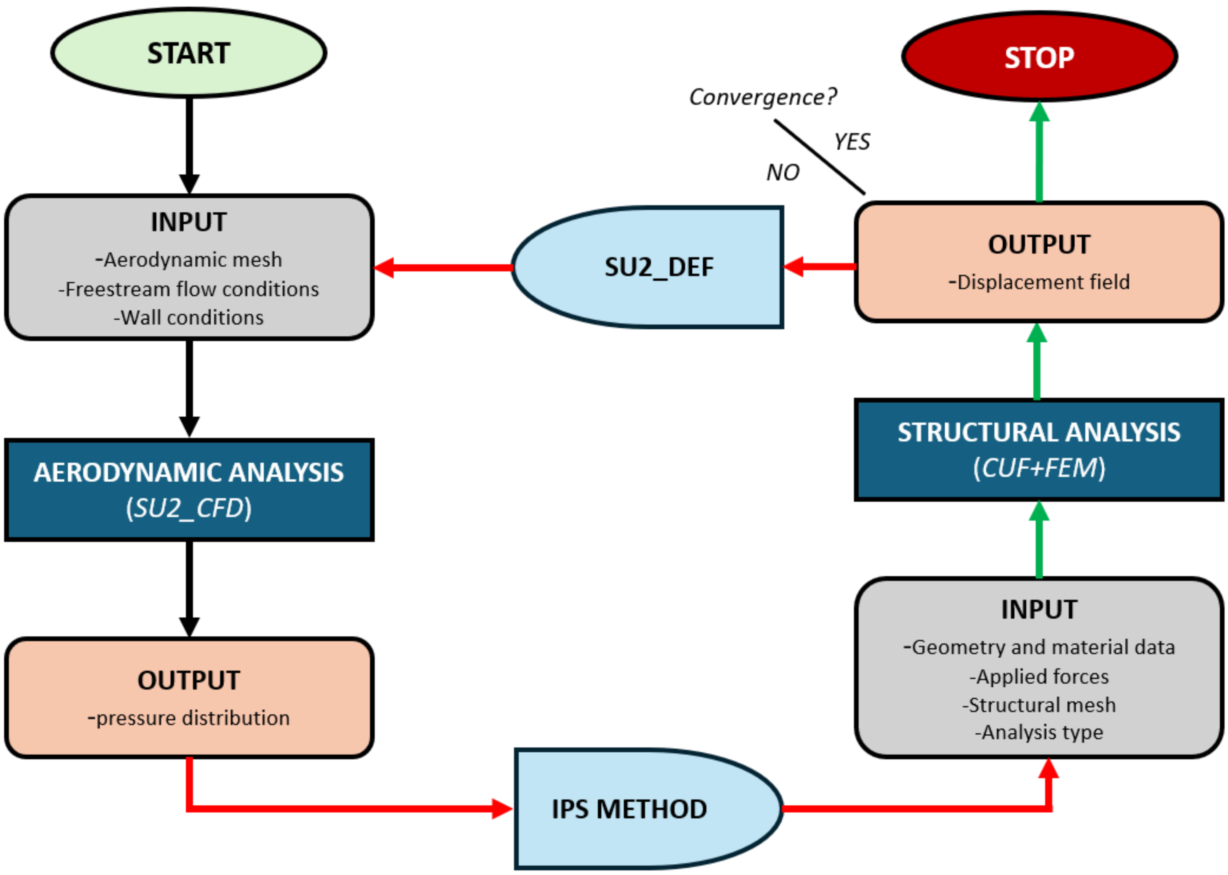


Figure 1: Schematic representation of the aeroelastic methodology.

## 3 Numerical results

This section presents linear static aeroelastic analyses conducted to assess the coupling between the aerodynamic and structural models. The aeroelastic analyses are examined through two dis-

| Theory | $V_\infty = 10$ m/s | | $V_\infty = 30$ m/s | | $V_\infty = 50$ m/s | |
|---|---|---|---|---|---|---|
| | SSA | SAA | SSA | SAA | SSA | SAA |
| EBBT/TBT | 8.301 | 8.320 | 71.674 | 67.310 | 197.908 | 186.308 |
| TE1 | 8.301 | 8.320 | 71.673 | 67.327 | 197.913 | 186.322 |
| TE2 | 7.571 | 7.510 | 65.413 | 67.655 | 180.588 | 223.457 |
| TE3 | 8.077 | 8.010 | 69.767 | 72.387 | 192.610 | 240.559 |
| TE4 | 8.056 | 8.028 | 70.153 | 72.682 | 194.096 | 241.005 |
| 2LE9 | 8.056 | 8.016 | 69.820 | 72.442 | 192.756 | 240.739 |

Table 1: Effect of the velocity on the transverse displacement of the leading edge of the wing tip $u_{z_{LE}}$ [mm] for different beam theories. Comparison between the SSA and SAA solutions with $\alpha = 1°$. Isotropic rectangular wing. 20B4 model.

tinct approaches: Static Structural Analysis (SSA), where aerodynamic loads are computed on the undeformed wing surface, and Static Aeroelastic Analysis (SAA), which accounts for the mutual interaction between fluid and structure. Specifically, SSA represents the first step in the iterative method, while the SAA solution is obtained upon method convergence. The cases include flat panels, swept wings, and more complex NACA airfoils, with attention to the influence of structural theory, velocity, and sweep angle. The results obtained using CFD are then compared and validated against reference values from the literature, as well as those derived from the classical aerodynamic approach, i.e., VLM. The aerodynamic validation of the framework is provided in the Appendix A. For completeness, the current framework does not allow for the direct calculation of the divergence velocity. However, divergence can be predicted by analyzing the structural response. By progressively increasing the free-flow velocity and monitoring the resulting deformations, it is possible to identify the onset of divergence within the CFD-CUF coupling when the displacements become excessive and the associated stresses exceed the material limits.

### 3.0.1 Isotropic rectangular wing

The first case considers a cantilever isotropic rectangular wing characterized by the following geometric and material properties: $b = 5$ m, $c = 1$ m, $t = 0.02$ m, $E = 69$ GPa, $\nu = 0.33$, and $\rho = 2700$ kg/m$^3$. Three different flow velocities $V_\infty = 10$, 30, and 50 m/s are considered, along with an angle of attack $\alpha = 1°$. The spacing $\Delta s$ $(y^+)$ of the aerodynamic mesh near the wall is dependent on flow velocity, necessitating the use of three distinct aerodynamic meshes. Specifically, the mesh for $V_\infty = 10$ m/s comprises 440878 elements, the one for $V_\infty = 30$ m/s consists of 423764 elements, and the mesh for $V_\infty = 50$ m/s contains 445017 elements. The structural modeling of the rectangular wing employs 20B4 elements along the $y$-axis, with various beam theories applied to the cross-section kinematics.

Table 1 provides the transverse displacement of the leading edge of the wing tip for different beam theories and using both the SSA and SAA approaches. The results indicate that both approaches produce comparable results at low speeds. However, as speed increases and structural deformations become more pronounced, the differences between the approaches become more evident. Additionally, the results obtained using high-order Taylor models closely match those derived from a quadratic Lagrange model. Figure 2 illustrates the convergence of the vertical displacement at the leading edge of the tip, $u_{z_{LE}}$, along with the relative error, $e(\Delta u_k)$, which represents the difference between the displacement at iteration $k$ and the preceding iteration $k-1$. As shown, the SAA method achieved convergence within 6 iterations at a velocity of $V_\infty = 50$ m/s. Table 2 shows the comparison between the TE4 (SAA) results and reference solutions [50, 45], including the percentage difference. Specifically, Ref. [50] employs a higher-order Equivalent Plate Model (EPM) coupled with CFD, whereas Ref. [45] utilizes refined 1D models within the VLM framework. For velocities of $V_\infty = 30$ m/s and 50 m/s, the iterative method yields solutions with percentage differ-

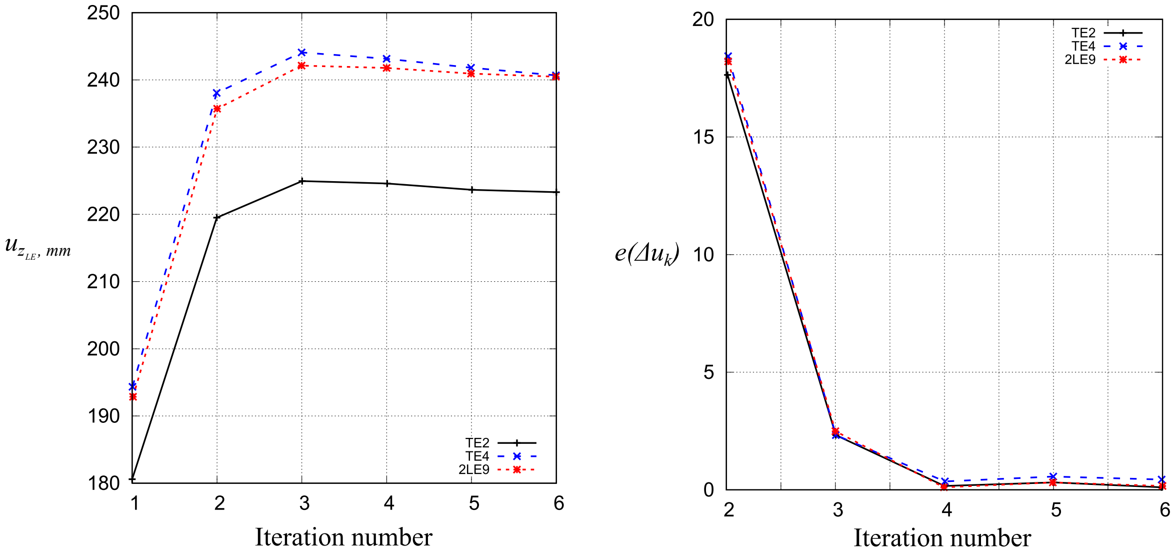


(a) $u_{z_{LE}}$

(b) $e(\Delta u_k)$

Figure 2: Aeroelastic convergence for the transverse displacement of the leading edge of the wing tip and the error in the iterative method for different kinematic theories. $V_\infty = 50$ m/s, $\alpha = 1°$. Isotropic rectangular wing.

| Model | $V_\infty = 10$ m/s | $V_\infty = 30$ m/s | $V_\infty = 50$ m/s |
|---|---|---|---|
| TE3 [50] | $5.811^{(38.14)}$ | $73.268^{(-0.80)}$ | $241.900^{(-0.37)}$ |
| TE4 [45] | $7.513^{(6.86)}$ | $73.397^{(-0.97)}$ | $244.460^{(-1.41)}$ |
| NASTRAN [45] | $7.545^{(6.40)}$ | $73.731^{(-1.42)}$ | $245.490^{(-1.83)}$ |
| TE4 | 8.028 | 72.682 | 241.005 |

Table 2: Comparison between the proposed solution and reference results for the transverse displacement of the leading edge of the wing tip $u_{z_{LE}}$ [mm]. Isotropic rectangular wing with $\alpha = 1°$. The percentage difference, $e(\Delta u_k)$, is reported in brackets.

| Velocity [m/s] | Theory | $u_{z_{LE}}$ [mm] | $u_{z_{TE}}$ [mm] | $\psi_{TIP}$ [°] |
|---|---|---|---|---|
| 10 | TE2 | 7.510 | 7.308 | 0.0116 |
| | TE3 | 8.010 | 7.805 | 0.0117 |
| | TE4 | 8.028 | 7.822 | 0.0118 |
| | 2LE9 | 8.016 | 7.811 | 0.0017 |
| | TE4* | 7.327 | 7.132 | 0.0112 |
| 30 | TE2 | 67.655 | 65.515 | 0.1226 |
| | TE3 | 72.387 | 70.214 | 0.1245 |
| | TE4 | 72.682 | 70.522 | 0.1238 |
| | 2LE9 | 72.442 | 70.267 | 0.1246 |
| | TE4* | 71.674 | 69.775 | 0.1088 |
| 50 | TE2 | 223.457 | 216.511 | 0.3979 |
| | TE3 | 240.559 | 233.485 | 0.4053 |
| | TE4 | 241.005 | 234.011 | 0.4007 |
| | 2LE9 | 240.739 | 233.661 | 0.4005 |
| | TE4* | 237.544 | 231.641 | 0.3554 |

Table 3: Effect of the velocity on the rotation at the tip section $\psi_{TIP}$ for different kinematic theories. Isotropic rectangular wing with $\alpha = 1°$. (* indicates a solution obtained with the VLM).

ences of only 1-2% compared to the reference data, demonstrating its ability to accurately capture the static aeroelastic response of the studied structure at these velocities. In contrast, the results exhibit greater deviations from other studies at $V_\infty = 10$ m/s. Notably, the limitations of the VLM method, used in [45], become more pronounced at this lower velocity, where viscous effects and the emergence of nonlinear flow phenomena, poorly captured by VLM, significantly impact aerodynamic loads. However, CFD methods also encounter difficulties in precisely modeling phenomena such as the laminar-to-turbulent flow transition, particularly in cases where the flow operates at very low Mach numbers. Table 3 presents the torsion values at the tip section of the structure for various velocities. These rotations are computed based on the vertical displacements measured at the leading edge, $u_{z_{LE}}$, and trailing edge, $u_{z_{TE}}$, using the following formula:

$$\psi_{TIP} = \arctan\left(\frac{u_{z_{LE}} - u_{z_{TE}}}{c}\right) \tag{26}$$

The results suggest that:

- The rotation angles are all positive, leading to an increase in incidence toward the wing tip due to the torsion;
- The rotation angle grows as the flow velocity increases. This trend is also illustrated in Fig. 3, which depicts the variation of $\psi_{TIP}$ with increasing velocity for the TE4 structural model;
- In every velocity regime, the classical aerodynamic models (VLM) underestimate the structural torsion compared to the CFD method;
- The static structural analysis, which does not account for fluid-structure interaction, underestimates the section's rotation. Therefore, implementing an aeroelastic model is essential for accurately capturing the structure's deformation field. The discrepancy between SAA and SSA analyses increases significantly with rising velocity.

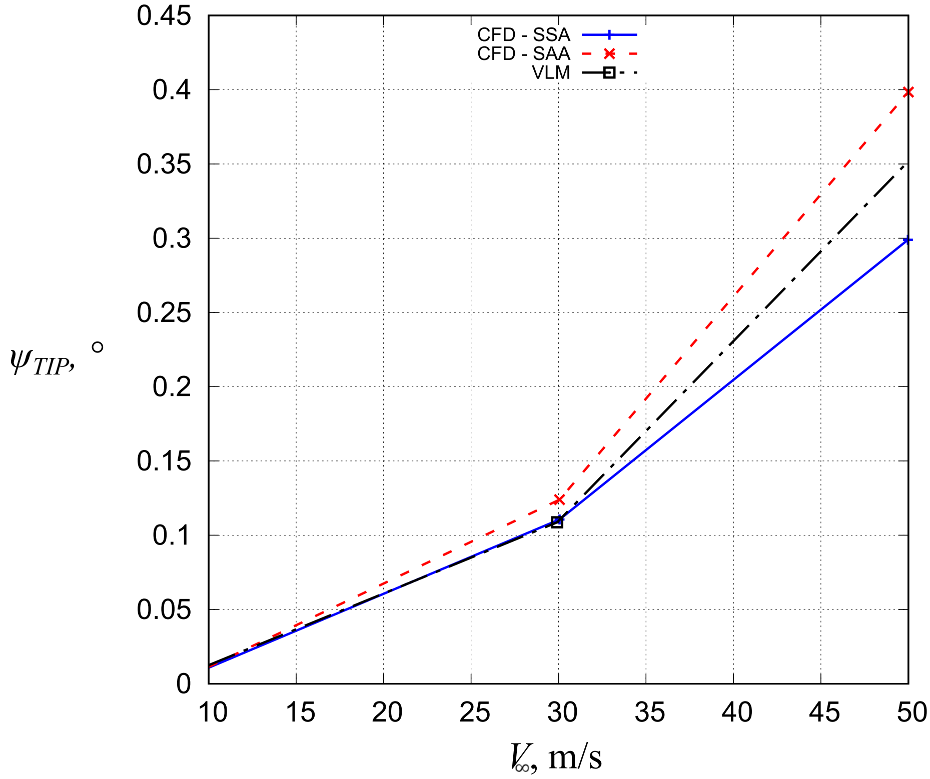


Figure 3: Effect of the velocity on the rotation at the tip section, $\psi_{TIP}$, for different aerodynamic models, using the TE4 structural model. Isotropic rectangular wing with $\alpha = 1$.

### 3.1 Swept wings

The following case examines the aeroelastic response of isotropic and composite swept wings, as illustrated in Fig. 4. Specifically, various wing geometries featuring a constant rectangular cross-section along the span were analyzed, considering sweep angles of $\Lambda$ = [-10°, 0°, 10°, 20°]. The

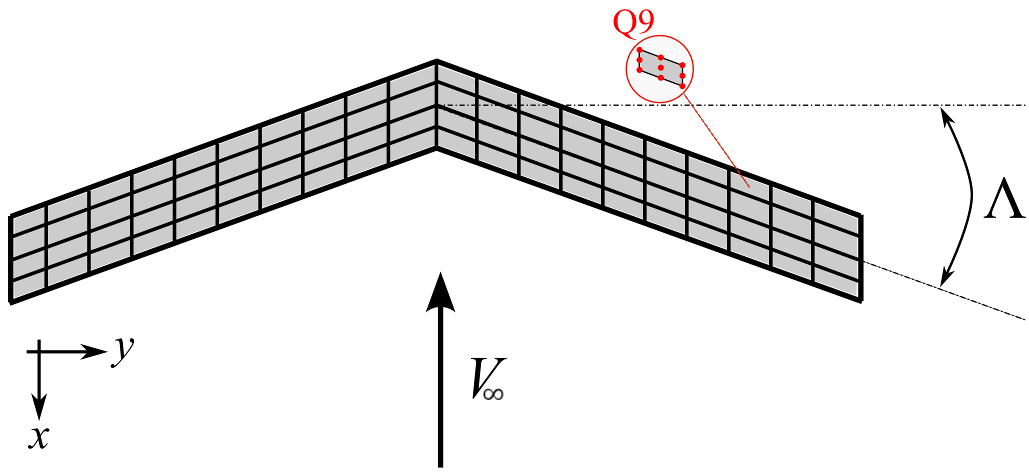


Figure 4: FE discretization of a swept-forward wing.

geometric characteristics of wingspan, chord, and thickness remain consistent with those of the wing analyzed in the previous case. An isotropic configuration is initially examined, characterized by the following material properties: $E = 69$ GPa, $\nu = 0.33$, and $\rho = 2700$ kg/m$^3$. The structural modeling of the swept wing employs a 4×20Q9 element mesh over the $x$-$y$ surface, see Fig. 4, while various plate theories are applied along the $z$-direction.

| Theory | $\Lambda$ [°] | $V_\infty = 10$ m/s | $V_\infty = 30$ m/s | $V_\infty = 50$ m/s |
|---|---|---|---|---|
| TE1 | -10 | 7.767 | 74.860 | 373.367 |
| | 0 | 6.895 | 62.205 | 209.099 |
| | 10 | 7.201 | 55.104 | 146.629 |
| | 20 | 7.772 | 54.824 | 124.407 |
| TE2 | -10 | 9.020 | 88.331 | 478.296 |
| | 0 | 8.010 | 72.200 | 242.897 |
| | 10 | 8.348 | 63.087 | 164.573 |
| | 20 | 8.971 | 61.900 | 137.537 |
| TE4 | -10 | 8.984 | 88.302 | 475.115 |
| | 0 | 7.992 | 72.208 | 242.953 |
| | 10 | 8.299 | 63.272 | 164.271 |
| | 20 | 8.915 | 62.039 | 137.257 |

Table 4: Effect of the sweep angle on the displacement at the leading edge of the tip of the wing $u_{z_{LE}}$ for different velocities and kinematic theories. Isotropic swept wing with $\alpha = 1°$. 4×20Q9 plate model.

Table 4 presents the influence of sweep angle on the transverse displacement at the wing tip's leading edge. The results indicates that increasing the positive sweep angle leads to a reduction in structural deflections. In contrast, a negative sweep angle has a significant negative effect on aeroelastic behavior, resulting in larger wing-tip displacements compared to a straight wing. Generally, displacements tend to increase with higher velocities. Regarding structural kinematic models, the results obtained from the first-order TE1 model deviate significantly from those derived using higher-order theories (TE2, TE4), mainly due to its inability to accurately evaluate the torsional behavior of the structure. The effect of the sweep angle on tip section rotation is presented in Table 5. The results confirms the stabilizing effect of positive sweep on aeroelastic behavior. Specifically, for $\Lambda = [10°, 20°]$, the tip rotation angles remain negative even at relatively high velocities. This leads to a decrease in the aerodynamic angle of attack compared to a straight wing, contributing to a stabilizing effect that increases the divergence speed of the lifting surface. Figure 5 illustrates the variation of $\psi_{TIP}$ and $u_{z_{LE}}$ with respect to freestream velocity for different sweep angles, along with a comparison of various kinematic theories. The results indicate that the TE1 model fails to reliably capture the structure's aeroelastic behavior. The figure underscores the importance of employing a higher-order model to accurately predict torsional effects. For the wing with a sweep angle of $\Lambda = 10°$, the tip section rotations exhibit a more pronounced discrepancy between the two models, leading to greater divergence in predicted bending behavior compared to the $\Lambda = 20°$ case. This difference occurs because aerodynamic loads significantly influence transverse displacements. Specifically, when the wing section rotates, its angle of attack increases, leading to higher aerodynamic loads. Considering the TE4 model, the effect of the sweep angle on the $u_{z_{LE}}$ and $\psi_{TIP}$ is reported in Fig. 6. The results highlight the stabilizing effect of positive sweep angles on aeroelastic behavior. As the velocity increases, wings with negative sweep angles, $\Lambda = -10°$, exhibit significantly higher transverse displacements and rotations, indicating greater susceptibility to aeroelastic deformation. In contrast, wings with positive sweep angles, $\Lambda = 10°$ or $20°$, demonstrate lower displacement and rotation variations, suggesting enhanced aerodynamic stability. The results reinforce the importance of sweep angle selection in mitigating aeroelastic instabilities, optimizing structural performance, and improving aerodynamic efficiency.

| Velocity [m/s] | Theory | $\Lambda$ [°] | $u_{z_{LE}}$ [mm] | $u_{z_{TE}}$ [mm] | $\psi_{TIP}$ [°] |
|---|---|---|---|---|---|
| 30 | TE1 | -10 | 74.860 | 69.485 | 0.3080 |
| | | 0 | 62.205 | 60.066 | 0.1225 |
| | | 10 | 55.104 | 55.500 | -0.0227 |
| | | 20 | 54.824 | 57.570 | -0.1573 |
| | TE2 | -10 | 88.331 | 82.401 | 0.3398 |
| | | 0 | 72.200 | 70.031 | 0.1243 |
| | | 10 | 63.087 | 63.756 | -0.0383 |
| | | 20 | 61.900 | 65.113 | -0.1841 |
| | TE4 | -10 | 88.302 | 82.383 | 0.3391 |
| | | 0 | 72.208 | 70.038 | 0.1243 |
| | | 10 | 63.272 | 63.960 | -0.0394 |
| | | 20 | 62.039 | 65.271 | -0.1852 |
| 50 | TE1 | -10 | 373.367 | 346.398 | 1.5449 |
| | | 0 | 209.099 | 201.762 | 0.4204 |
| | | 10 | 146.629 | 147.368 | -0.0423 |
| | | 20 | 124.407 | 130.274 | -0.3362 |
| | TE2 | -10 | 478.296 | 446.155 | 1.8409 |
| | | 0 | 242.897 | 235.428 | 0.4279 |
| | | 10 | 164.573 | 165.985 | -0.0809 |
| | | 20 | 137.537 | 144.266 | -0.3855 |
| | TE4 | -10 | 475.115 | 443.122 | 1.8324 |
| | | 0 | 242.953 | 235.479 | 0.4282 |
| | | 10 | 164.271 | 165.747 | -0.0845 |
| | | 20 | 137.257 | 144.021 | -0.3876 |

Table 5: Effect of the sweep angle on the rotation at the tip section, $\psi_{TIP}$, for different velocities and plate theories. Isotropic swept wing with $\alpha = 1°$. 4×20Q9 plate model.

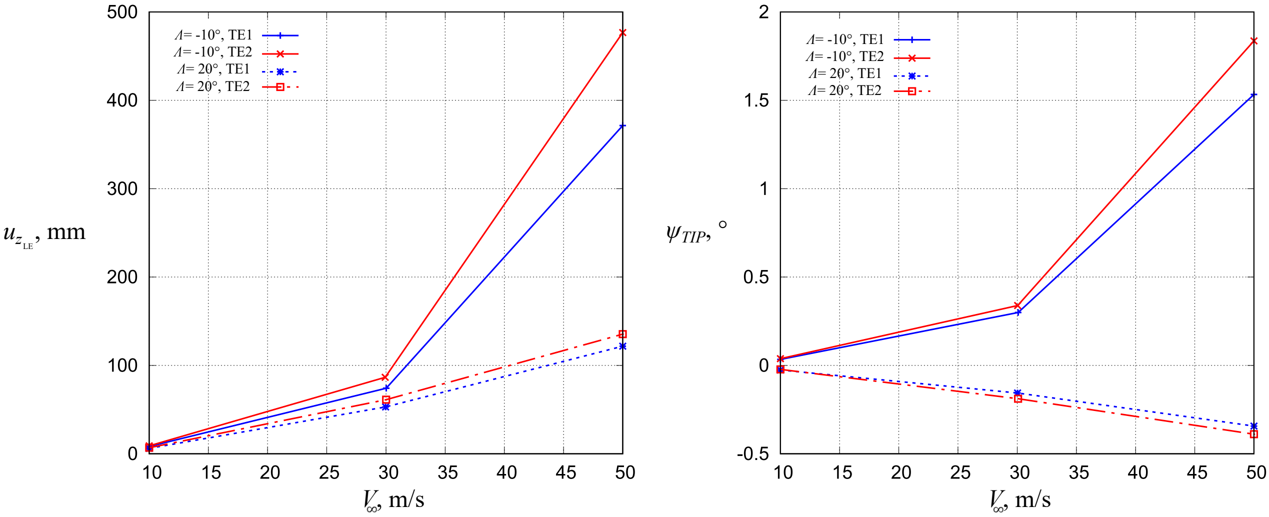


(a) (b)

Figure 5: Effect of the velocity on the displacement at the leading edge of the tip of the wing, $u_{z_{LE}}$, and rotation at the tip section, $\psi_{TIP}$, for different sweep angles and plate theories. Isotropic swept wing with $\alpha = 1°$. 4×20Q9 plate model.

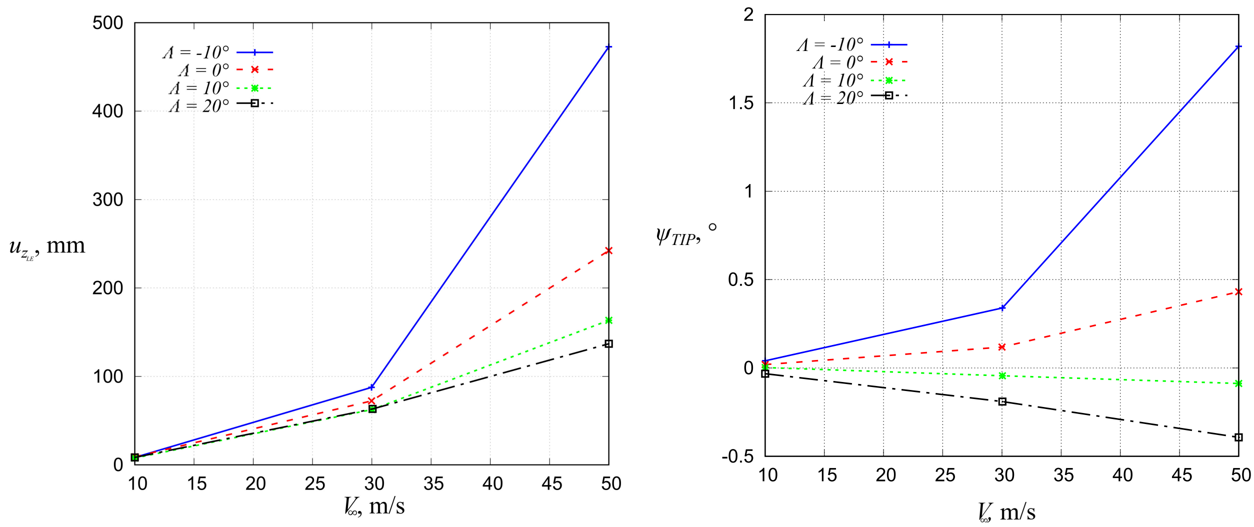


(a) (b)

Figure 6: Effect of the sweep angle on the displacement at the leading edge of the tip of the wing, $u_{z_{LE}}$, and rotation at the tip section, $\psi_{TIP}$. Isotropic swept wing with $\alpha = 1°$. 4×20Q9+TE4 plate model.

## 3.2 Thin-walled NACA 2415 airfoil

The last case considers the static aeroelastic analysis of an unswept, untapered, isotropic wing ($E = 69$ GPa, $\nu = 0.33$) featuring a NACA 2415 airfoil section. The half-wing has a span length of $b = 5$ m, while the selected cross-section is a thin-walled NACA 2415 airfoil. The section is divided into three cells by two longerons aligned along the span direction, positioned at 25% and 75% of the chord, as depicted in Fig. 7. The wing, subjected to a flow with varying speeds of $V_\infty = 5, 10, 30, 50$

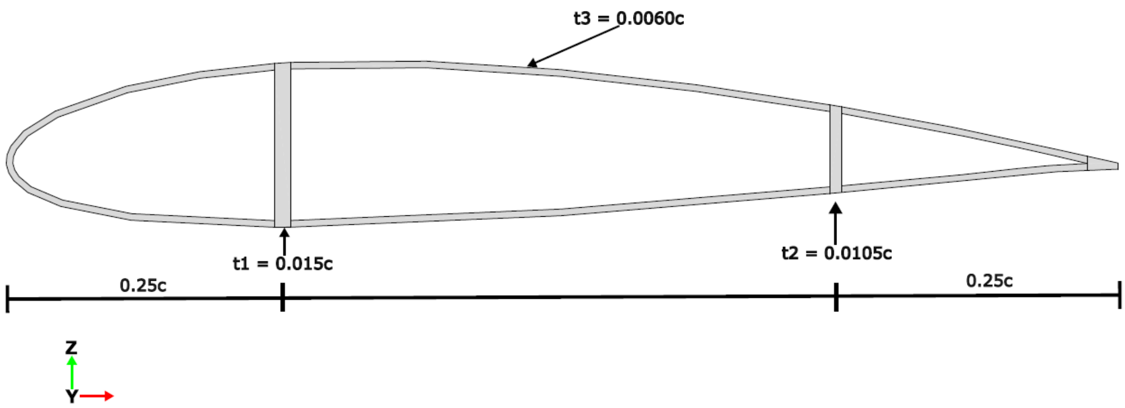


Figure 7: Reference frame and geometry of the NACA 2415 wing configuration.

m/s at an angle of attack $\alpha = 3°$, is modeled using 20B4 elements along the beam axis and adopting various structural theories in the cross-section. Figure 8 illustrates the aerodynamic and FEM mesh discretization of the analyzed wing structure.

Table 6 and Figure 9 show the transverse displacements at the leading edge of the wing tip, along with the rotation of the tip section, across various beam theories and velocities. Table 7 shows the aerodynamic coefficients $C_L$ and $C_D$ for different velocities, considering both the SAA and SSA approaches. The results indicate that the drag coefficient ($C_D$) decreases as the velocity ($V_\infty$) increases for both the SSA and SAA approaches (Fig. 10a). In contrast, the lift coefficient

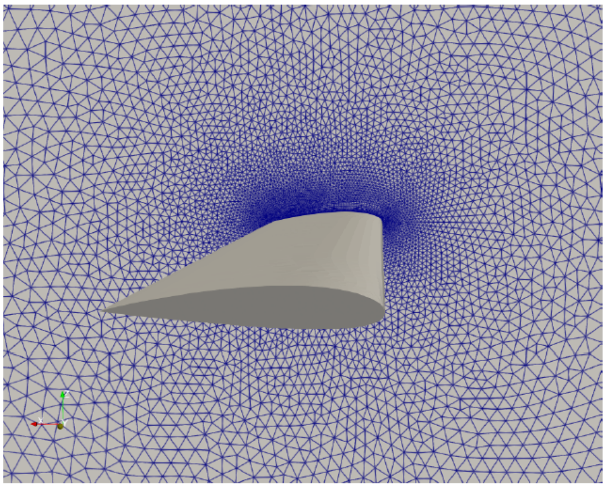

(a) CFD mesh

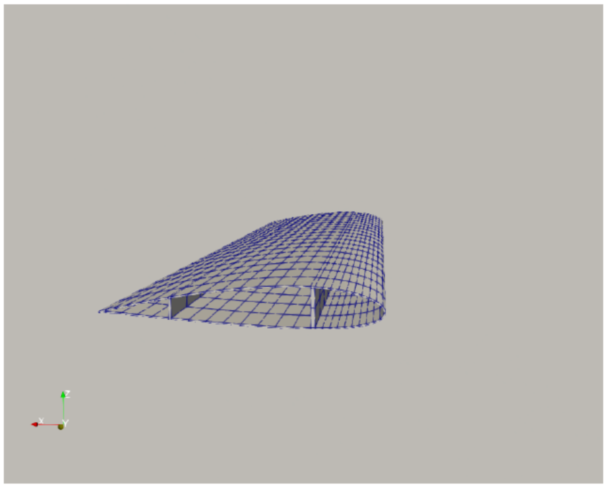

(b) FEM mesh

Figure 8: (a) Aerodynamic and (b) structural mesh discretization for the NACA 2415 wing configuration.

| Theory | | $V_\infty = 10$ m/s | $V_\infty = 30$ m/s | $V_\infty = 50$ m/s |
|---|---|---|---|---|
| EBBT | $u_{z_{LE}} \times 10^3$ | 0.3661 | 3.2964 | 8.9719 |
| | $\psi_{TIP} \times 10^4$ | -(*) | -(*) | -(*) |
| TBT | $u_{z_{LE}} \times 10^3$ | 0.3664 | 3.3054 | 8.9812 |
| | $\psi_{TIP} \times 10^4$ | -(*) | -(*) | -(*) |
| TE1 | $u_{z_{LE}} \times 10^3$ | 0.3627 | 3.2605 | 9.0522 |
| | $\psi_{TIP} \times 10^4$ | 0.2869 | 4.1851 | 8.0832 |
| TE5 | $u_{z_{LE}} \times 10^3$ | 0.3596 | 3.2302 | 8.9687 |
| | $\psi_{TIP} \times 10^4$ | 0.9320 | 7.1833 | 13.4346 |
| LE9 | $u_{z_{LE}} \times 10^3$ | 0.3649 | 3.2842 | 9.1002 |
| | $\psi_{TIP} \times 10^4$ | 0.8209 | 6.7961 | 12.6625 |

Table 6: Transverse displacements of the leading edge at the wing tip and the rotation of the tip section for different thickness values. NACA 2415 wing with $\alpha = 3°$. (* indicates that the torsion is not considered by classical theories, i.e., EBBT, TBT.)

| | | $V_\infty = 5$ m/s | $V_\infty = 10$ m/s | $V_\infty = 30$ m/s | $V_\infty = 50$ m/s |
|---|---|---|---|---|---|
| $C_L$ | SSA | 0.4410 | 0.4581 | 0.4831 | 0.4911 |
| | SAA | 0.4377 | 0.4580 | 0.4746 | 0.4630 |
| $C_D$ | SSA | 0.0990 | 0.0605 | 0.0296 | 0.0225 |
| | SAA | 0.0100 | 0.0627 | 0.2934 | 0.0232 |

Table 7: Aerodynamic coefficients $C_L$ and $C_D$ for different velocities using SAA and SSA approaches. NACA 2415 wing with $\alpha = 3°$.

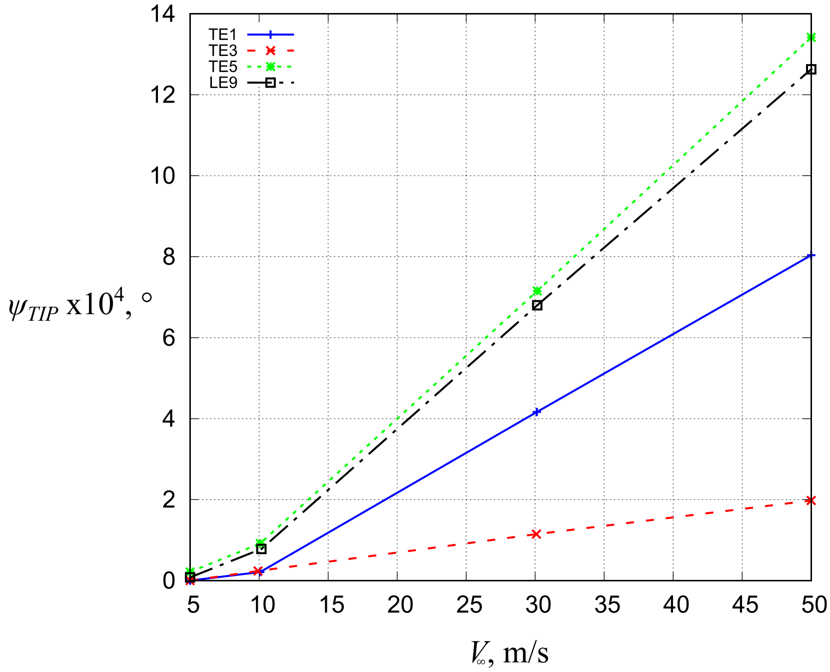


Figure 9: Tip section rotations of the NACA 2415 wing as a function of the velocity for various beam theories.

($C_L$) increases with velocity ($V_\infty$) for the SSA method. However, in the SAA approach, $C_L$ begins to decrease beyond $V_\infty = 30$ m/s (Fig. 10b), likely due to premature local flow separations on the wing profile. This phenomenon results from an increased local angle of attack, defined as $\alpha_{loc} = \alpha + \psi(y)$, where $\alpha$ is the imposed angle of attack and $\psi(y)$ represents the torsion angle induced by fluid-structure interaction. Finally, Fig. 11 illustrates the distribution of the local lift coefficient along the wingspan of the NACA 2415 wing, considering both SSA and SAA approaches. Specifically, the local lift coefficient for a span-wise segment $\Delta y$ is defined as $C_l = C_p \sin(\alpha_{loc})\Delta y$, where $C_p$ represents the pressure coefficient of the profile. Instead, the total lift coefficient is given by $C_L = \int_0^b C_p(y)\sin(\alpha_{loc}(y))\, dy$. To better highlight the differences between the SSA and SAA approaches, Fig. 12 presents the variation in the local lift coefficient, $\Delta C_l$, defined as $\Delta_{C_l} = \frac{C_{l,SAA} - C_{l,SSA}}{C_{l,SAA}}$. The results reveal a difference between the static (SSA) and aeroelastic (SAA) distributions of the lift coefficient ($C_L$), caused by a local increase in the angle of attack ($\alpha_{loc}$). This increase is induced by structural torsion resulting from fluid-structure interaction.

# 4 Conclusions

This paper addresses the identified gap in the literature regarding the integration of one-dimensional (1D) structural models with computational fluid dynamics (CFD). Previous studies have mainly focused on coupling CFD with classical two-dimensional (2D) or three-dimensional (3D) models, while refined one-dimensional (1D) and 2D models have been employed only in combination with classical aerodynamic methods, such as the Vortex Lattice Method (VLM) or the Doublet Lattice Method (DLM). To fill this gap, the present work applies the Carrera Unified Formulation (CUF) to develop variable kinematic 1D and 2D finite elements, which are then integrated with open-source CFD software to perform static aeroelastic analyses of various wing structures. The structural and aerodynamic models are coupled through a fluid-structure interaction (FSI) algorithm based on the Infinite Plate Spline (IPS) method. The static aeroelastic response of straight and swept wings was evaluated through an iterative coupling procedure. The study examines the influence of key parameters, including geometry, structural theory, aerodynamic modeling, freestream velocity,

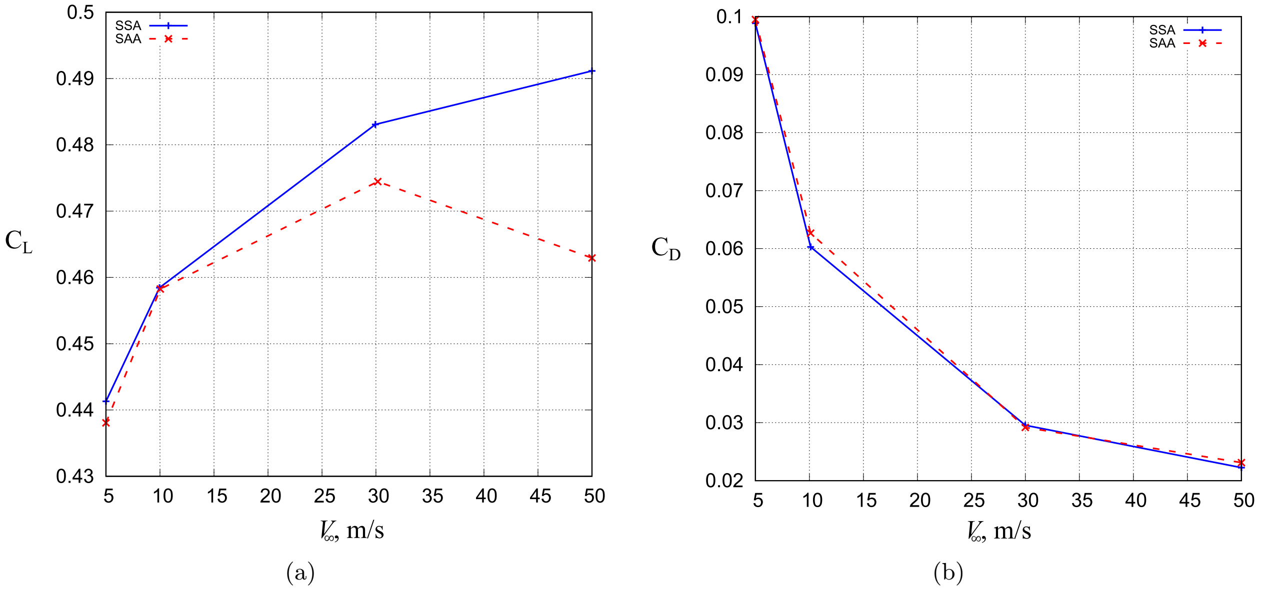


Figure 10: (a) $C_L$ and (b) $C_D$ versus $V_\infty$ using both SSA and SAA approaches for the NACA 2415 wing configuration with $\alpha = 3°$.

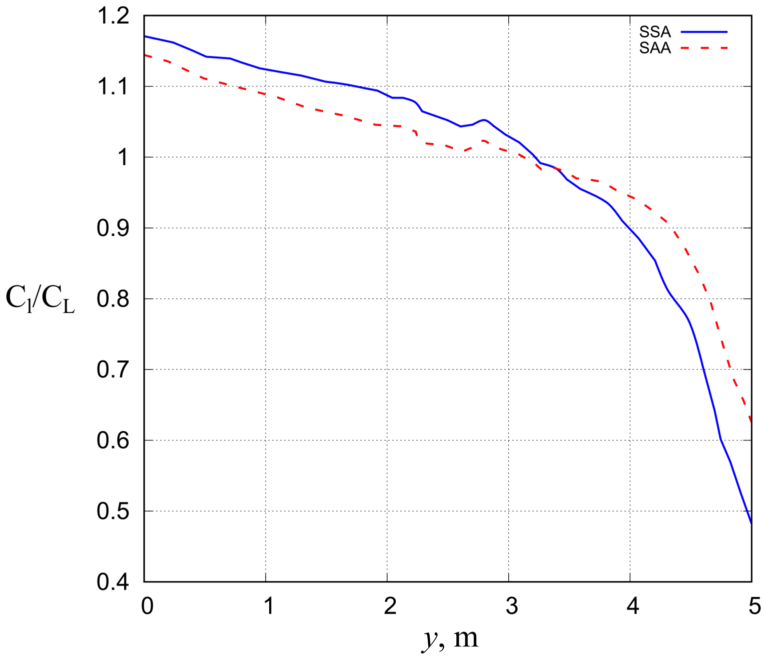


Figure 11: Distribution of the local lift coefficient along the wingspan using SSA and SAA approaches for the NACA 2415 wing configuration.

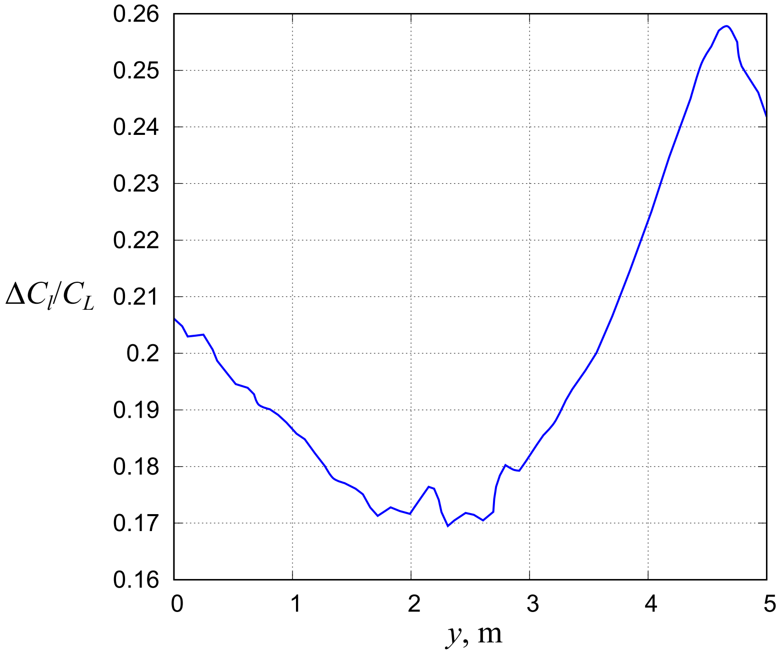


Figure 12: Difference between SSA and SAA in the distribution of the local lift coefficient along the wingspan for the NACA 2415 wing configuration.

and sweep angles. Validation against established literature confirms the methodology's robustness, flexibility, and potential for aeroelastic applications. The following main conclusions can be drawn:

- The results underscore the importance of employing a high-order structural model to accurately capture the torsional behavior of the structure. Specially, classical beam theories such as Euler-Bernoulli and Timoshenko fail to capture torsional effects and complex deformation modes. Higher-order models, such as TE4 or LE9, are recommended for accurately predicting structural response;

- Altough VLM computations are orders of magnitude faster than CFD, the direct resolution of the Navier-Stokes equations using a CFD code guarantees greater accuracy compared to classical methods. The study finds that CFD-based approaches yield 2–5% higher accuracy for moderate velocities, with deviations exceeding 10% in high-speed, highly deformable cases due to aerodynamic complexities that VLM cannot capture;

- As speed increases, significant discrepancies emerge between the static structural and static aeroelastic approaches, highlighting the limitations of the former in aeroelastic studies. The static structural method computes aerodynamic forces on an undeformed wing surface without accounting for fluid-structure interaction or iterative corrections. In contrast, the static aeroelastic approach integrates fluid-structure coupling, refining the solution through successive iterations until convergence is reached. The static structural analysis tends to underestimate structural deformation, as it disregards aeroelastic interactions entirely. On the other hand, the static aeroelastic analysis captures these coupling effects, resulting in displacements up to 20–30% larger than those predicted by the static method at high speeds. These differences emphasize the necessity of iterative FSI approaches for realistic and accurate aeroelastic design assessments;

- The evaluations carried out on the combined effect of sweep angles on the aeroelastic behavior of the structure have highlighted the versatility and reliability of the proposed aeroelastic model. This framework proves to be an effective tool for the preliminary design of aeronautical structures.

- Although CFD remains the dominant contributor to the overall computational effort, the use of refined 1D CUF-based structural models with 3D capabilities significantly reduces the cost compared to shell or solid discretization. This efficiency is particularly relevant when analyzing complex airfoils and nonlinear regimes, making the framework suitable for preliminary design studies.

Future research will focus on aeroelastic studies of complex composite wing configurations, including geometric nonlinearity and rotating blade analyses.

## References


[1] D.H. Hodges and G.A. Pierce. *Introduction to structural dynamics and aeroelasticity*. Cambridge University Press, 2011.

[2] Y.C. Fung. *An introduction to the theory of aeroelasticity*. Courier Dover Publications, 2008.

[3] E.H. Dowell, H.C. Curtiss, R.H. Scanlan, and F. Sisto. *A modern course in aeroelasticity*. Springer, 1995.

[4] M.T. Bordogna, P. Lancelot, D. Bettebghor, and R. De Breuker. Static and dynamic aeroelastic tailoring with composite blending and manoeuvre load alleviation. *Structural and Multidisciplinary Optimization*, 61(5):2193–2216, 2020.

[5] O. Stodieck, J.E. Cooper, P.M. Weaver, and P. Kealy. Optimization of tow-steered composite wing laminates for aeroelastic tailoring. *AIAA Journal*, 53(8):2203–2215, 2015.

[6] B. Zhang, K. Chen, and L. Zu. Aeroelastic tailoring method of tow-steered composite wing using matrix perturbation theory. *Composite Structures*, 234:111696, 2020.

[7] G. Quaranta, P. Masarati, J. Serafini, and M. Gennaretti. Aeroelastic rotorcraft-pilot couplings: problems and methods. *Aerotecnica Missili & Spazio*, 95(3):176–187, 2016.

[8] M.A. Alam, H.H. Ya, S.M. Sapuan, O. Mamat, B. Parveez, M. Yusuf, F. Masood, and R.A. Ilyas. Recent advancements in advanced composites for aerospace applications: a review. *Advanced Composites in Aerospace Engineering Applications*, pages 319–339, 2022.

[9] J.F. Sigrist. *Fluid-structure interaction: an introduction to finite element coupling*. John Wiley & Sons, 2015.

[10] L. Demasi. *Introduction to Unsteady Aerodynamics and Dynamic Aeroelasticity*. Springer, 2024.

[11] G.P. Guruswamy. A review of numerical fluids/structures interface methods for computations using high-fidelity equations. *Computers & Structures*, 80(1):31–41, 2002.

[12] P. Cicala. Le azioni aerodinamiche su profili di ala oscillanti in presenza di corrente uniforme. *R. Accad. Torino*, 2, 1934.

[13] G. Ellenberger. Bestimmung der luftkräfte auf einen ebenen tragflügel mit querruder. *Zeitschrift für Angewandte Mathematik und Mechanik*, 16(4):199–226, 1936.

[14] H.G. Küssner. Zusammenfassender bericht über den instationären auftrieb von flügeln. *Luftfahrtforschung*, 13:410, 1936.

[15] T. von Kármán and J.M. Burgers. General aerodynamic theory, perfect fluids. aerodynamic theory. *Aerodynamic Theory*, 2, 1934.

[16] T. Theodorsen. General theory of aerodynamic instability and the mechanism of flutter. *NACA Report*, 1979.

[17] R. Yurkovich. Status of unsteady aerodynamic prediction for flutter of high-performance aircraft. *Journal of Aircraft*, 40(5):832–842, 2003.

[18] D.M. Schuster, Danny D. Liu, and L.J. Huttsell. Computational aeroelasticity: success, progress, challenge. *Journal of Aircraft*, 40(5):843–856, 2003.

[19] H. Joshi and P. Thomas. Review of vortex lattice method for supersonic aircraft design. *The Aeronautical Journal*, 127(1317):1869–1903, 2023.

[20] E. Albano and W.P. Rodden. A doublet-lattice method for calculating lift distributions on oscillating surfaces in subsonic flows. *AIAA Journal*, 7(2):279–285, 1969.

[21] J. Katz and A. Plotkin. *Low-speed aerodynamics*. Cambridge University Press, 2001.

[22] D. Anderson, J.C. Tannehill, R.H. Pletcher, R. Munipalli, and V. Shankar. *Computational fluid mechanics and heat transfer*. McGraw–Hill, New York, 2020.

[23] R.L. Harder and R.N. Desmarais. Interpolation using surface splines. *Journal of Aircraft*, 9(2):189–191, 1972.

[24] G. Quaranta, P. Masarati, and P. Mantegazza. A conservative mesh-free approach for fluid-structure interface problems. In *International Conference on Computational Methods for Coupled Problems in Science and Engineering*, 2005.

[25] M.H. Shirk, T.J. Hertz, and T.A. Weisshaar. Aeroelastic tailoring-theory, practice, and promise. *Journal of Aircraft*, 23(1):6–18, 1986.

[26] O.C. Zienkiewicz and R.L. Taylor. *The finite element method for solid and structural mechanics*. Elsevier, 2005.

[27] T.A. Weisshaar. Divergence of forward swept composite wings. In *20th Structures, Structural Dynamics, and Materials Conference*, page 722, 1979.

[28] L. Librescu and O. Song. On the static aeroelastic tailoring of composite aircraft swept wings modelled as thin-walled beam structures. *Composites Engineering*, 2(5-7):497–512, 1992.

[29] Z. Qin and L. Librescu. Aeroelastic instability of aircraft wings modelled as anisotropic composite thin-walled beams in incompressible flow. *Journal of Fluids and Structures*, 18(1):43–61, 2003.

[30] J. Murua, R. Palacios, and J.M.R. Graham. Applications of the unsteady vortex-lattice method in aircraft aeroelasticity and flight dynamics. *Progress in Aerospace Sciences*, 55:46–72, 2012.

[31] M. Dagilis and S. Kilikevičius. Aeroelasticity model for highly flexible aircraft based on the vortex lattice method. *Aerospace*, 10(9):801, 2023.

[32] A. Tamer and P. Masarati. Aeroelastic stability estimation of control surfaces with freeplay nonlinearity. *Aerotecnica Missili & Spazio*, 96:154–164, 2017.

[33] V. Gulizzi and I. Benedetti. Computational aeroelastic analysis of wings based on the structural discontinuous Galerkin and aerodynamic vortex lattice methods. *Aerospace Science and Technology*, 144:108808, 2024.

[34] A.C. Gray and J.R. Martins. A proposed benchmark model for practical aeroelastic optimization of aircraft wings. In *AIAA SciTech 2024 Forum*, page 2775, 2024.

[35] R.K. Kapania and S. Raciti. Recent advances in analysis of laminated beams and plates. Part I-Sheareffects and buckling. *AIAA Journal*, 27(7):923–935, 1989.

[36] R.K. Kapania and S. Raciti. Recent advances in analysis of laminated beams and plates, Part II: Vibrations and wave propagation. *AIAA Journal*, 27(7):935–946, 1989.

[37] J.N. Reddy. *Mechanics of laminated composite plates and shells: theory and analysis.* New York: CRC Press, 2004.

[38] E. Carrera. Evaluation of layerwise mixed theories for laminated plates analysis. *AIAA Journal*, 36(5):830–839, 1998.

[39] K.K. Gupta. Development of a finite element aeroelastic analysis capability. *Journal of Aircraft*, 33(5):995–1002, 1996.

[40] J.A.A. Lyrio, D.A. Rade, and J.L.F. Azevedo. High-fidelity fluid-structure interaction applied to static aeroelasticity in transonic flows. *Aerospace Science and Technology*, 153:109477, 2024.

[41] M. Mangano, S. He, Y. Liao, D.G. Caprace, A. Ning, and J.R. Martins. Aeroelastic tailoring of wind turbine rotors using high-fidelity multidisciplinary design optimization. *Wind Energy Science Discussions*, 2023:1–33, 2023.

[42] E. Carrera, M. Cinefra, M. Petrolo, and E. Zappino. *Finite Element Analysis of Structures through Unified Formulation.* John Wiley & Sons, Chichester, West Sussex, UK, 2014.

[43] A. Varello, E. Carrera, and L. Demasi. Vortex lattice method coupled with advanced one-dimensional structural models. *Journal of Aeroelasticity and Structural Dynamics*, 2(2), 2011.

[44] A. Varello, A. Lamberti, and E. Carrera. Static aeroelastic response of wing-structures accounting for in-plane cross-section deformation. *International Journal of Aeronautical and Space Sciences*, 14(4):310–323, 2013.

[45] E. Carrera, A. Varello, and L. Demasi. A refined structural model for static aeroelastic response and divergence of metallic and composite wings. *CEAS Aeronautical Journal*, 4:175–189, 2013.

[46] M. Petrolo. Advanced 1D structural models for flutter analysis of lifting surfaces. *International Journal of Aeronautical and Space Sciences*, 13(2):199–209, 2012.

[47] M. Petrolo. Flutter analysis of composite lifting surfaces by the 1D Carrera Unified Formulation and the doublet lattice method. *Composite Structures*, 95:539–546, 2013.

[48] M. Filippi and E. Carrera. Aerodynamic and mechanical hierarchical aeroelastic analysis of composite wings. *Mechanics of Advanced Materials and Structures*, 23(9):997–1004, 2016.

[49] M. Grifò, V. Gulizzi, A. Milazzo, A. Da Ronch, and I. Benedetti. High-fidelity aeroelastic transonic analysis using higher-order structural models. *Composite Structures*, 321:117315, 2023.

[50] M. Grifò, A. Da Ronch, and I. Benedetti. A computational aeroelastic framework based on high-order structural models and high-fidelity aerodynamics. *Aerospace Science and Technology*, 132:108069, 2023.

[51] F. Goetten, D.F. Finger, M. Marino, C. Bil, M. Havermann, and C. Braun. A review of guidelines and best practices for subsonic aerodynamic simulations using RANS CFD. In *Asia Pacific International Symposium on Aerospace Technology*, pages 227–245, 2019.

[52] T.D. Economon, F. Palacios, S.R. Copeland, T.W. Lukaczyk, and J.J. Alonso. SU2: An open-source suite for multiphysics simulation and design. *AIAA Journal*, 54(3):828–846, 2016.

| Geometrical parameters | |
|---|---|
| Chord ($c$) | 0.264 m |
| Wingspan ($b$) | 0.804 m |
| Thickness ($t$) | 6 mm |
| Area ($S$) | 0.2122 m$^2$ |
| Taper ratio ($\lambda$) | 1 |

Table 8: Geometrical characteristic of the wing structure with AR = 3.


[53] P. Spalart and S. Allmaras. A one-equation turbulence model for aerodynamic flows. In *30th Aerospace Sciences Meeting and Exhibit*, page 439, 1992.

[54] G.K. Ananda, P.P. Sukumar, and M.S. Selig. Measured aerodynamic characteristics of wings at low Reynolds numbers. *Aerospace Science and Technology*, 42:392–406, 2015.

[55] A. Pelletier and T.J. Mueller. Low Reynolds number aerodynamics of low-aspect-ratio, thin/flat/cambered-plate wings. *Journal of Aircraft*, 37(5):825–832, 2000.

[56] M. Shields and K. Mohseni. Effects of sideslip on the aerodynamics of low-aspect-ratio low-Reynolds-number wings. *AIAA Journal*, 50(1):85–99, 2012.

[57] K. Malik, W. Asrar, and E. Sulaeman. Low Reynolds number numerical simulation of the aerodynamic coefficients of a 3D wing. *International Journal of Aviation, Aeronautics, and Aerospace*, 5(1):8, 2018.


# A Aerodynamic model validation

This study considers a wing structure with an Aspect Ratio (AR) of 3, representative of the wings used in Unmanned Aerial Vehicles (UAVs) and Micro Air Vehicles (MAVs). The considered case is inspired by well-known works [54, 55, 56, 57]. The geometric characteristics are detailed in Table 8, while Fig. 13 illustrates a schematic representation of the model employed. Particular emphasis is placed on evaluating key simulation parameters, including mesh quality and far-field extension.

The wing has a constant rectangular cross-section with triangular leading and trailing edges,

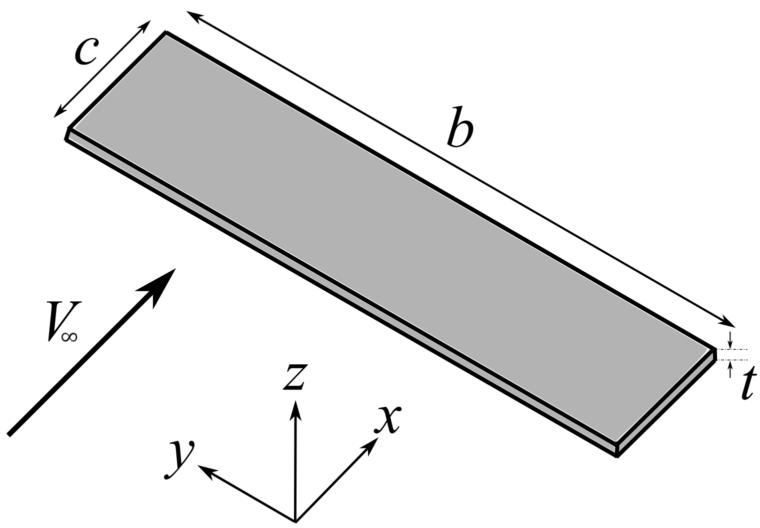


Figure 13: Wing structure model with AR = 3.

designed to optimize airflow management at non-zero angles of attack. This aspect is illustrated

| Aerodynamic parameters | |
|---|---|
| $Re$ | 80000 |
| $\mu$ | $1.7988\times10^{-5}$ Pa/s |
| $T_\infty$ | 288.15 K |
| $p_\infty$ | 101359 Pa |
| $\rho_\infty$ | 1.225 kg/m$^3$ |
| $V_\infty$ | 4.4498 m/s |
| $M_\infty$ | 0.013 |

Table 9: Aerodynamic flow parameters for the considered problem. Wing with AR = 3.

in Fig. 14, which also depicts the aerodynamic mesh employed in the analysis. The flow that hits the wing is in standard atmospheric conditions and is characterized by a Re = 80000. Despite the

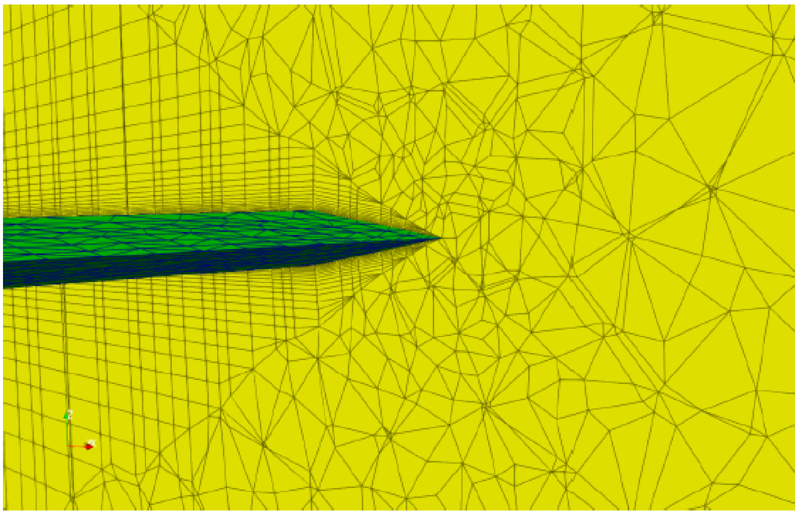

Figure 14: Aerodynamic mesh of the wing with AR = 3.

low Reynolds number, the small wingspan leads to pronounced 3D flow effects, which play a crucial role in determining aerodynamic forces, stability, boundary layer transition, and the formation of recirculation bubbles. Table 9 summarizes the key characteristics of the problem and the parameters of the undisturbed flow, denoted by the subscript "$\infty$". Additionally, flow separation occurs at high angles of attack, leading to a transition into a turbulent regime.

A single wing was analyzed within a hemispherical domain to minimize the aerodynamic mesh size, applying appropriate symmetry conditions, as depicted in Fig. 15. The initial phase of the study focused on assessing the quality of the computational grid, particularly the influence of the parameter $y^+$ and the extension of the far-field. Using an angle of attack $\alpha = 5°$ as a reference, a convergence analysis was conducted by varying the first wall cell size $\Delta s$ and the dimensions of the computational domain. The aerodynamic problem was solved in SU2, employing the RANS equations with the Spalart-Allmaras turbulence model. Starting from an estimated $y^+$ value and applying the procedure reported in Section 2.2, the first wall cell dimension $\Delta s$ was determined. To ensure reliable aerodynamic coefficients $C_L$ and $C_D$, a $y^+$ value of 0.1 was selected, corresponding to a cell height of $\Delta s = 6.48\times10^{-3}$ mm. The boundary layer was discretized using 33 layers with an average growth rate of 1.4, providing adequate refinement near the body, as illustrated in Fig. 16. The region closest to the body consists of anisotropic prismatic cells (green), while the outer region is composed of isotropic tetrahedral cells (red). In the transition zone, pyramidal cells (yellow) facilitate the gradual shift between these two structures. The second parameter considered is the far-field extension, defined in terms of a characteristic length of the analyzed model, in this case the wing

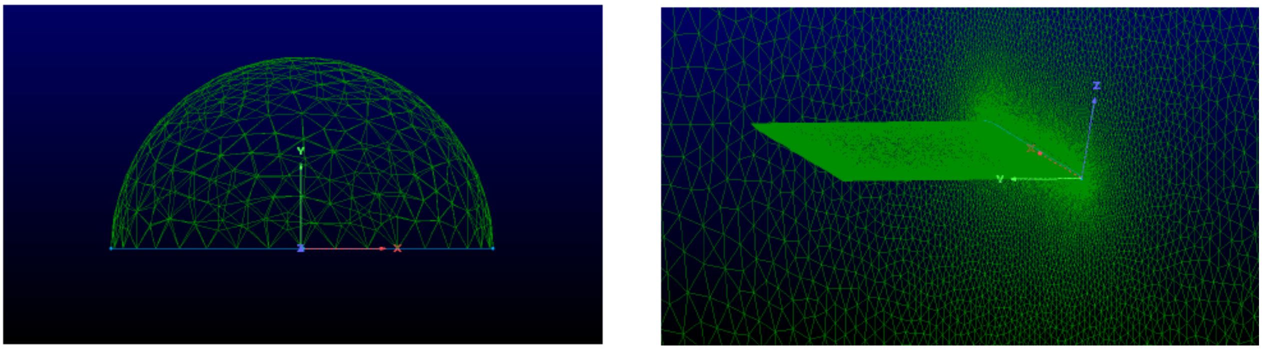

(a) Hemispherical domain (b) Wing structure clamped in the symmetry plane

Figure 15: Representation of the aerodynamic mesh for the wing with AR = 3.

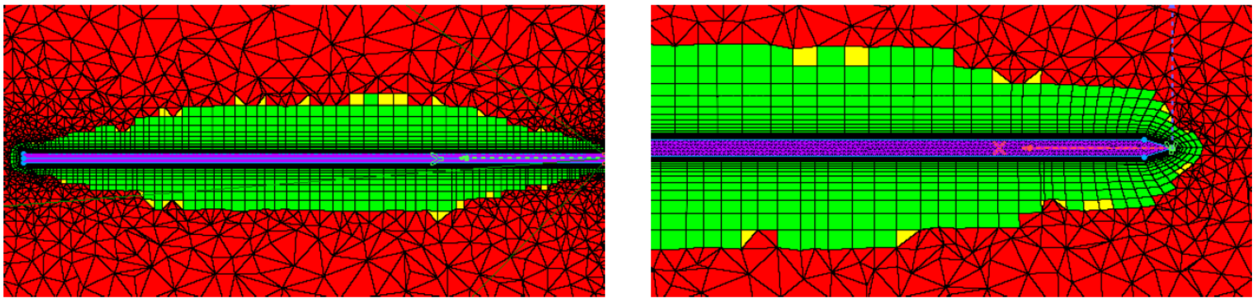

(a) Section along $x$-axis (b) Section along $y$-axis

Figure 16: Details of the aerodynamic mesh near the wall. Wing with AR = 3.

chord. Figure 17 presents the convergence analysis conducted by varying the far-field size, expressed in multiples of the aerodynamic chord. The results indicate sensitivity to boundary-condition-induced perturbations when the far-field measures 10 or 30 times the chord length. Notably, the lift coefficient exhibits greater fluctuations compared to the drag coefficient. Increasing the far-field size leads to the stabilization of both coefficients, as evidenced by the flattening of the $C_L$ and $C_D$ curves in Fig. 17. However, this improvement comes at the expense of a larger mesh size, resulting in greater computational demands and extended convergence times. An 50-times chord far-field offers an optimal trade-off between accuracy and computational efficiency. Therefore, a domain with an 50-times chord extension was selected for subsequent analyses to balance simulation accuracy with computational cost.

Figure 18 illustrates the effect of the angle of attack ($\alpha$) on the aerodynamic coefficients. The SU2 software results exhibit excellent correlation with existing literature, encompassing both numerical [57] and experimental studies [54, 55, 56]. Specifically, for the lift coefficient, as illustrated in Fig. 18a, slight deviations from experimental data are primarily observed near the stall condition and at the maximum $C_L$. These discrepancies can be attributed to geometric differences between the simulated and experimental models. In contrast, Fig. 18b demonstrates that the SU2 drag coefficient results align perfectly with both the numerical findings of Malik *et al.* [57] and the experimental data from Ananda *et al.* [54].

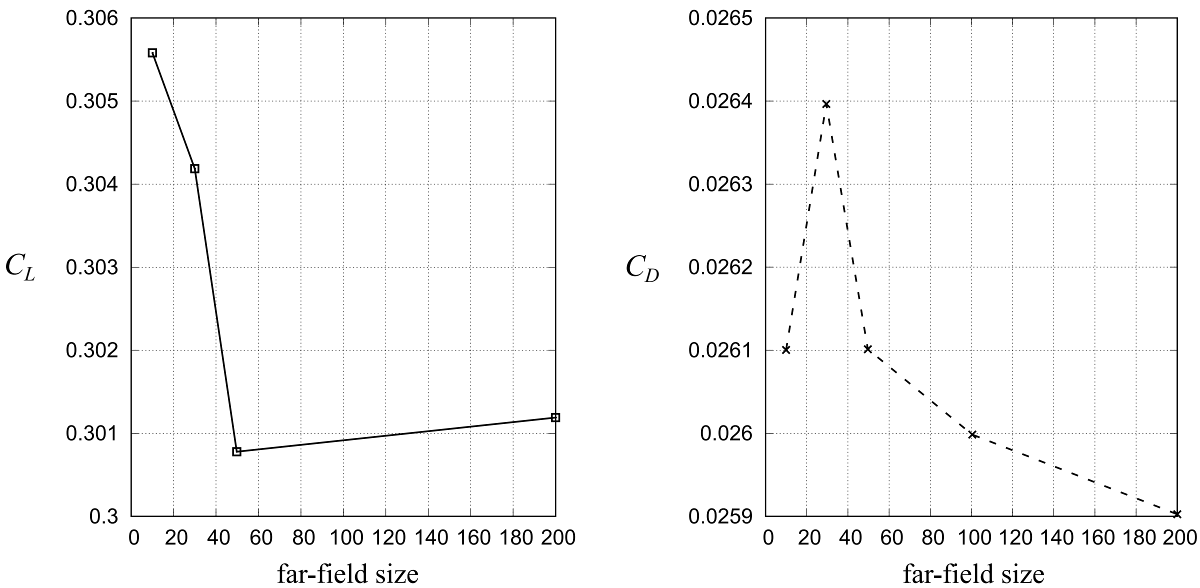


(a) $C_L$

(b) $C_D$

Figure 17: Convergence analysis on aerodynamic coefficients as a function of the domain extension. Wing with AR = 3.

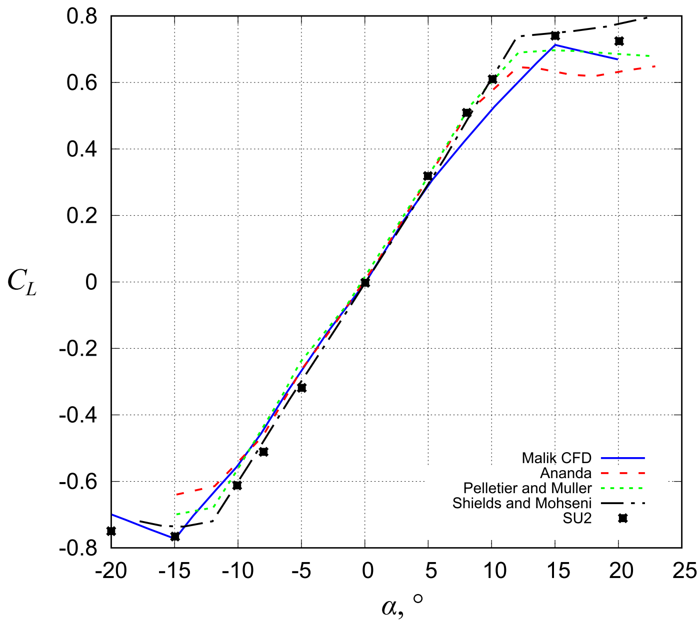


(a) $C_L - \alpha$

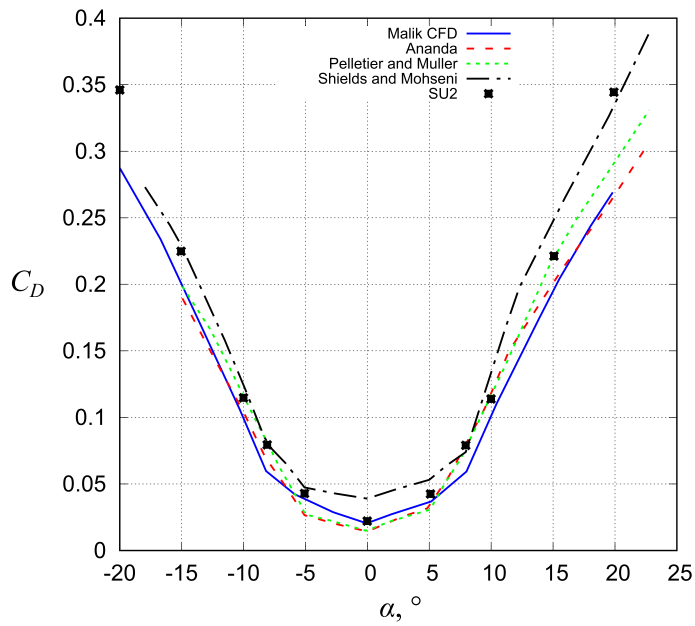


(b) $C_D - \alpha$

Figure 18: Variation of $C_L$ and $C_D$ with respect to the angle of attack $\alpha$. Wing structure with AR = 3.